Available online at www.sciencedirect.com
ScienceDirect
Journal of Nuclear Materials 374 (2008) 32–43
journal of nuclear materials
www.elsevier.com/locate/jnucmat

Simulation with DIONISIO 1.0 of thermal and mechanical pellet-cladding interaction in nuclear fuel rods

Alejandro Soba, Alicia Denis *

Departamento Combustibles Nucleares, Comisión Nacional de Energía Atómica, Avenida del Libertador 8250, 1429 Buenos Aires, Argentina

Received 18 January 2007; accepted 14 June 2007

Abstract

The code DIONISIO 1.0 describes most of the main phenomena occurring in a fuel rod throughout its life under normal operation conditions of a nuclear thermal reactor. Starting from the power history, DIONISIO predicts the temperature distribution in the domain, elastic and plastic stress and strain, creep, swelling and densification, release of fission gases, caesium and iodine to the rod free volume, gas mixing, pressure increase, restructuring and grain growth in the UO_2 pellet, irradiation growth of the Zircaloy cladding, oxide layer growth on its surface, hydrogen uptake and the effects of a corrosive atmosphere either internal or external. In particular, the models of thermal conductance of the gap and of pellet-cladding mechanical interaction incorporated to the code constitute two realistic tools. The possibility of gap closure (including partial contact between rough surfaces) and reopening during burnup is allowed. The non-linear differential equations are integrated by the finite element method in two-dimensions assuming cylindrical symmetry. Good results are obtained for the simulation of several irradiation tests.

1. Introduction

The DIONISIO code performs the calculations in the *r*–*z* domain illustrated in Fig. 1. It generates, when rotated around the *z* axis, a segment of a nuclear power reactor fuel pin corresponding to one half of a pellet.

The strain analysis of the pellet and the cladding considers the elastic and plastic regimes and includes thermal expansion, swelling, densification, creep and irradiation growth of the cladding for sufficiently long periods [1,2]. Due to thermal expansion and to the mechanical restrictions of the pellet, it experiences a non-uniform deformation: the initially cylindrical pellet surface distorts, bending outwards, with a radius increase larger at the top and bottom faces than at the central belt [3]. If the pellet deformation is sufficiently large, it may come into contact with the cladding (pellet-cladding mechanical interaction - PMCI), particularly in regions next to the pellet–pellet contact surfaces.

The effect of fission products of gas nature, mainly Xe and Kr, is included through the intra and intergranular bubbles which form due to the low solubility of these atoms in the oxide lattice. The intergranular bubbles accumulate gas until they reach a saturation level. After that, the gas in excess is released to the plenum, the gap and the dishing. In this manner, the fission gases contribute to increasing the internal pressure in the fuel rod, modify the gap thickness and decrease the thermal conductance of the gap, which is reflected in further temperature increase. The fission gas inventory is obtained as the solution of the diffusion equation of gas in a spherical grain of UO_2 [1,4,5].

The fission products, either solid or gaseous, dissolved in the UO_2 matrix and both types of gas bubbles occupy a volume larger than that of the original material and produce pellet swelling that obey different laws according to the case.

The high temperature at the pellet center and the steep thermal gradient across the pellet radius also generate grain growth and pores migration towards the pellet center. The

* Corresponding author.
E-mail address: denis@cnea.gov.ar (A. Denis).

0022-3115/$ - see front matter © 2007 Elsevier B.V. All rights reserved.
doi:10.1016/j.jnucmat.2007.06.020

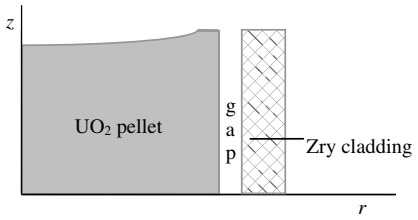

Fig. 1. System pellet-gap-cladding analyzed in DIONISIO.

consequent fuel restructuring is evidenced by the presence, at the end of life (EOL), of radial zones with different grain size and morphology: columnar grains at the center, large equiaxed grains in the middle zone, and fine as-fabricated grains at the external pellet ring. Besides that, fuel cracks, either radial or axial, develop in the pellet with the effect of making it appear as constituted of a softer material.

The code presented here takes account of these phenomena. It solves first the heat diffusion equation taking as input data the power history and the boundary conditions: a fixed temperature at the external surface of the fuel element and temperature gradient equal to zero at the pellet center line. The temperature distribution in the pellet, the gap and the cladding is thus obtained. To this end, a finite element scheme in cylindrical coordinates is used. The temperature dependence of the fuel thermal conductivity is responsible for the non-linearity of the thermal problem. This imposes the need of an iterative procedure to calculate the temperature at each node. With the same discretization and with the results of the thermal step, the stress–strain problem is solved. Plasticity and creep render this calculation also non-linear.

The code also calculates pore migration, grain growth and differential restructuring in the fuel, the amount of fission products in the internal atmosphere of the rod, hydrogen uptake by the cladding that contribute to the strain hardening, and oxide growth on the external cladding surface that is responsible for the time dependence of the boundary condition of the thermal problem.

The purpose of this work is to present the DIONISIO code describing the models included in it with special emphasis in those relative to thermal conductance of the gap and to PCMI. The code can simulate rods with or without a gap and the possibility of gap closure and reopening during burnup is also allowed. When the gap is open heat transfer is verified through the gas phase composed by a gas mixture. With a closed gap, the roughness of pellet and cladding surfaces determines that heat exchange be accomplished partly through the solid–solid contact spots and partly through the gas phase confined among them. All these considerations contribute to obtaining realistic thermal predictions. The model of PCMI evaluates the contact force between both interacting surfaces, predicts their displacements and modifies the surfaces shape to avoid overlap. This tool also gives a significant contribution to the good quality of the results. The models of thermal and mechanical pellet-cladding interaction have been separately checked before introducing them in DIONISIO. The results of these tests are also included in the present work.

2. General models

2.1. The thermal problem

The temperature distribution in each rod material is obtained by solving the differential equation in cylindrical coordinates

$$\frac{1}{r}\frac{\partial}{\partial r}\left(rk_r^j(T)\frac{\partial T}{\partial r}\right)+\frac{\partial}{\partial z}\left(k_z^j(T)\frac{\partial T}{\partial z}\right)=-Q^j(r) \tag{1}$$

where T represents the temperature, $k^j(T)$ is the thermal conductivity of material j in the r and z direction and Q^j is the volumetric heat generation rate given by

$$Q^j=\begin{cases}Q^f & \text{in the } UO_2 \text{ fuel pellet}\\ 0 & \text{other material.}\end{cases} \tag{2}$$

It is generally accepted that heating due to γ radiation represents less than about 5% of the total energy involved in the different processes that take place in the reactor core [6] and is not considered in this model. Q^f changes with time according to the power history. The boundary conditions are

$$\left.\frac{\partial T}{\partial r}\right|_{r=0}=0;\quad h_{fc}\left[T(r_{ef})-T(r_{ic})\right]=\frac{P_l(z)}{2\pi r_{ef}};\qquad k^c(T)\left.\frac{\partial T}{\partial r}\right|_{r=r_{ic}}=-\frac{P_l(z)}{2\pi r_{ic}};\quad T(r_{ec})=T_C(z) \tag{3}$$

where $P_l(z)=\pi r_{\mathrm{ef}}^2 Q^f(z)$ is the lineal power, r_{ef}, r_{ic} and r_{ec} are the external and internal radii of the fuel and the cladding. The external cladding temperature $T_{\mathrm{C}}(z)$ is calculated from the coolant temperature $T_{\mathrm{R}}(z)$, the thermal jump at the rod-coolant interface and the temperature variation through the cladding oxide layer [7,8]. h_{fc} is the thermal conductance of the gap between the fuel and cladding surfaces; it contains the contributions of three terms: $h_{\mathrm{fc}}=h_{\mathrm{rad}}+h_{\mathrm{gas}}+h_{\mathrm{s}}$, where h_{rad} is due to radiation effects, h_{gas} expresses the contribution of the gaseous atmosphere in the gap and h_{s} represents the contribution of the solid portions of surface in contact and is different to zero when the gap is partially or totally close.

DIONISIO also allows selecting a pellet with a central hole. In this situation, an additional heat diffusion equation is needed for this gas phase, with a thermal conductivity of a gas mixture type and null power generation.

2.2. The stress–strain analysis

Given the axial symmetry of the system, neither the geometry nor the surface loadings depend on the angular coordinate. The displacements, strains and stresses are functions of r and z only. If u and w represent the displacements in the r and z directions, respectively, the strain-displacement relations are [9]:

$$e_{rr} = \frac{\partial u}{\partial r}; e_{\theta\theta} = \frac{u}{r}; e_{zz} = \frac{\partial w}{\partial z}; e_{rz} = \frac{\partial u}{\partial z} + \frac{\partial w}{\partial r}; e_{r\theta} = 0;$$
$$e_{z\theta} = 0. \quad (4)$$

The column vector $\{e\}$ contains the non-zero components of the strain:

$$\{e\}^{\mathrm{T}} = [\, e_{rr} \quad e_{\theta\theta} \quad e_{zz} \quad e_{rz} \,] \quad (5)$$

where the superscript T indicates the transpose. It has different contributions depending on the material. For the cladding, it is given by

$$\{e\}^{c} = \{\varepsilon_{\mathrm{th}}\} + \{\varepsilon_{\mathrm{el}}\} + \{\varepsilon_{\mathrm{pl}}\} + \{\varepsilon_{\mathrm{cr}}\} + \{\varepsilon_{\mathrm{ig}}\} \quad (6)$$

where the terms stand for the thermal, elastic, plastic, creep and irradiation growth strains, respectively. For the fuel pellet, it is

$$\{e\}^{\mathrm{f}} = \{\varepsilon_{\mathrm{th}}\} + \{\varepsilon_{\mathrm{el}}\} + \{\varepsilon_{\mathrm{pl}}\} + \{\varepsilon_{\mathrm{cr}}\} + \{\varepsilon_{\mathrm{sw}}\} + \{\varepsilon_{\mathrm{d}}\} \quad (7)$$

with a similar meaning of the terms, except for the inclusion of the swelling $\{\varepsilon_{\mathrm{sw}}\}$ and densification $\{\varepsilon_{\mathrm{d}}\}$ contributions.

The elastic strain and the stress are related for each material by the Hooke's law

$$\{\sigma\} = [D]\{\varepsilon_{\mathrm{el}}\} \quad (8)$$

where $[D]$ is the material matrix. Its elements are functions of the Young's modulus and the Poisson's ratio. The values adopted are listed in Table 1. The components of the stress are:

$$\{\sigma\}^{T} = [\, \sigma_{rr} \quad \sigma_{\theta\theta} \quad \sigma_{zz} \quad \sigma_{rz}]. \quad (9)$$

The values of E were taken from Refs. [10,11], μ from [12], α from [11], k from [13,14] and σ_{Y} from [12].

When the finite element method is applied, the unknown displacements u and w are written in terms of the element nodal values and the shape functions. The differential Eq. (4) are thus transformed to linear equations, which are formally similar to those for the thermal problem.

The thermal strain is defined as:

$$\{\varepsilon_{\mathrm{th}}\}^{\mathrm{T}} = [\, \alpha\Delta T \quad \alpha\Delta T \quad \alpha\Delta T \quad 0 \,] \quad (10)$$

where α is the thermal expansion coefficient of the corresponding material. Swelling and densification also give origin to strain vectors without shear component. The corresponding strain term contains three contributions to swelling: intragranular and grain boundary bubbles and lattice fission products. The models used in DIONISIO are listed in Table 2.

$$\varepsilon_{\mathrm{sw}} + \varepsilon_{\mathrm{d}} = \frac{1}{3}\left[\left.\frac{\Delta V}{V}\right|_{\mathrm{int.bub.}} + \left.\frac{\Delta V}{V}\right|_{\mathrm{g.b.bub.}} + \left.\frac{\Delta V}{V}\right|_{\mathrm{l.f.p.}} + \left.\frac{\Delta V}{V}\right|_{\mathrm{dens.}}\right]. \quad (11)$$

The plastic term is obtained by a recursive procedure in which the values of stress and strain are fitted to the uniaxial curve corresponding to the material involved. In the case of the present study, in the temperature range considered, only the Zry exhibits a significant plastic deformation.

The model of fuel creep adopted [10] assumes that the creep rate depends on the power regime, either steady state or ramp [15]. Depending on the stress state, the main term in the pellet creep rate law is either linear or proportional to a power of the stress. The transition stress is defined as $\sigma_{\mathrm{t}} = \frac{1.6547\times10^{7}}{g^{0.5714}}$, where g is the grain size in μm [10]. The creep and irradiation growth models for Zircaloy included in DIONISIO were taken from Refs. [16] and [17], respectively. The models for swelling and densification were taken from Refs. [1,4,5].

3. PCI in DIONSIO

3.1. Thermal contact

As the temperature distribution and the heat removal regime are the conditioning steps for the rest of the phenomena, determination of the thermal conductivity of the materials involved deserves special attention. A large amount of work has been devoted to this aspect in connection with the fuel and cladding materials, for which there exist fully valid models. However, some questions are still pending in connection with gap conductance in two essential aspects. On the one hand, there are few experimental data. On the other hand, not any single theoretical model is able to simulate the variety of conditions in which the

Table 1
Material properties used in the code; T: temperature (K); P: porosity

Young's modulus, E (Pa)	UO_2: $2.334\times10^{11}(1-2.752P)(1-1.0915\times10^{-4}T)$ Zry: $1.236\times10^{11} - 6.221\times10^{7}T$
Poisson's ratio, μ	UO_2: $1.045 - 1.7025T + 0.9265T^2$ Zry: 0.32
Thermal expansion, α (K^{-1})	UO_2: $(-4.972\times10^{-4} + 7.107\times\ 10^{-6}T + 2.583\times10^{-9}T^2)/\Delta T$ Zry: $(-2.07\times10^{-3} + 6.72\times10^{-6}T)/\Delta T$
Thermal conductivity, k ($Wm^{-1}\,K^{-1}$)	UO_2: $\frac{1}{0.03494+2.243\times10^{-4}T} + \frac{6.157\times10^{9}}{T^2}\exp\left[-\frac{2.256\times10^{-19}}{kT}\right]$ Zry: $7.51 + 2.09\times10^{-2}T - 1.45\times10^{-5}T^2 + 7.67\times10^{-9}T^3$ Gap: gas mixing model
Yield stress, σ_Y (Pa)	UO_2: $108000\times10^{-T/1225}$ Zry: $6.578\times10^{4}(1 - 1.686\times10^{-3}T + 7.748\times10^{-7}T^2)$

Table 2
Models used in DIONISIO

Creep law for UO_2 [10] $\dot{\varepsilon}$: creep rate (s^{-1}); $a_1 - a_8$ constants; $\dot{f}$: fission rate (fiss./m^3 s); σ: applied stress (Pa); g: grain size (μm); Q_1, Q_2 y Q_3: activation energies (J/mol); R: universal gas constant (J/mol K); D: percent of theoretical density.	$\dot{\varepsilon} = \frac{(a_1+a_2\dot{f})\sigma \exp(-Q_1/RT)}{(a_3+D)g^2} + \frac{(a_4+a_8\dot{f})\sigma^{4.5}\exp(Q_2/RT)}{a_6+D} + a_7\sigma\dot{f}\exp(Q_3/RT)$
Creep law for Zry [16] k, b and c constants, ε_{eq}: generalized creep strain; $\sigma_{\theta\theta}$: hoop stress (Pa); ϕ: neutron flux (n/m^2 s)	$\dot{\varepsilon} = \frac{(2a_1a_2a_3)^2}{\varepsilon_{eq}}; a_1 = k\phi; a_2 = \exp\left(-\frac{5035}{RT}\right); a_3 = \sigma_{\theta\theta} + b\exp(c\sigma_{\theta\theta})$
Cladding irradiation growth [17] ϕ: fast neutrons flux (n/m^2 s)	$d\varepsilon^{Ig}_{zz}/dt = 4.942\times10^{-20}\phi$ $d\varepsilon^{Ig}_{rr}/dt = -0.941\, d\varepsilon^{Ig}_{zz}/dt$ $d\varepsilon^{Ig}_{\theta\theta}/dt = -0.059\, d\varepsilon^{Ig}_{zz}/dt$
Swelling due to intragranular bubbles [1,4,5] C_B: concentration of intragranular bubbles; R_B: bubble radius	$\frac{\Delta V}{V}\Big\vert_{int.bub.} = \frac{(4/3)\pi R_B^3 C_B}{1-(4/3)\pi R_B^3 C_B} \approx (4/3)\pi R_B^3 C_B$
Swelling due to intergranular bubbles [1,4,5] P_{ext}: external pressure (Pa); $2\gamma/r_f$: stress due to surface tension; a: grain radius (m); r_f: radius of curvature of the bubble's face (m); N: surface concentration of gas atoms (at/m^2); k: Boltzmann constant (J/K)	$\frac{\Delta V}{V}\Big\vert_{g.b.bub} = \frac{3kTN}{2a(2\gamma/r_f+P_{ext})}$
Swelling due to fission products in the fuel lattice [11] Bup: burnup (at%U^{235} consumed)	$\frac{\Delta V}{V}\Big\vert_{l.f.p.} = 0.0032\,Bup$
Densification [17] b: rate of bubbles resolution (s^{-1}); P_0: initial porosity	$\frac{\Delta V}{V}\Big\vert_{dens.} = -\frac{P_o(1-e^{-bt})}{1-P_o e^{-bt}} \approx -P_o(1-e^{-bt})$

Temperatures T in K.

gap may appear during the fuel lifetime within a reactor. These conditions depend on the fuel element design, its component materials and on the power history. The release of gaseous fission products during burnup increases the internal pressure of the element, which may range from few atmospheres at the beginning to 77–100 atm at the end of life. The low thermal conductivity of the released products provokes a gradual temperature increase in the element during the irradiation time, as the gas composition varies. According to the fuel element design the gap may remain open during most of its history or it may close to produce pellet-cladding contact. In the latter case, the conductance of the gap depends on properties like roughness and hardness of both surfaces. The involved variables take values between wide possible ranges: for example, the contact pressure (parameter difficult to state), may vary from a few MPa to 50 MPa. A general review of the known models for the thermal conductance between UO_2 and Zry for both, open and closed gap, is found in Ref. [18].

Generally speaking, if the gap is open heat transport from the pellet to the cladding occurs by the contributions of heat conduction through the gas phase filling the gap and that of radiation from the solid surfaces. If it is closed, heat is transported by conduction, partly through the regions of pellet-cladding solid contact and partly through the gas phase filling the regions where solid contact is not made.

3.1.1. Thermal conductance of the gas phase

The gas atmosphere in the gap, assumed to be initially constituted by He only, modifies its composition during burnup due to the incorporation of fission gases, mainly Xe and Kr. Heat conduction through the gas mixture filling the pellet-cladding gap is the dominant mechanism of transfer. The gas conductivity is given by functions like [11,19]:

$$k_i = A_i T^{B_i} \tag{12}$$

where A_i and B_i are constants and $i =$ He, Xe, Kr, other. The gas composition is then a time function. The conductivity of the mixture is calculated in DIONISIO as [10]:

$$k_{gasmix} = \sum_{i=1}^{n} \beta_i x_i \tag{13}$$

with

$$\beta_i = k_i \left[x_i + \sum_{\substack{j=1 \\ j\neq i}}^{n} \psi_{ij} x_j \right]^{-1} \tag{14}$$

where M_i and x_i are the molecular weight and fraction of species i, and

$$\psi_{ij} = \phi_{ij}\left[1 + 2.41\frac{(M_i - M_j)(M_i - 0.142M_j)}{(M_i+M_j)^2}\right] \tag{15}$$

$$\phi_{ij} = 2^{-3/2}\left(1+\frac{M_i}{M_j}\right)^{-1/2}\left(1+\left(\frac{k_i}{k_j}\right)^{1/2}\left(\frac{M_i}{M_j}\right)^{1/4}\right)^2. \tag{16}$$

The phenomena described in Section 2.2 induce variations in the gap width. If it is wider than the mean free path of the gas molecules, the conductance of the gas phase in the gap takes the simple formula:

$$h_{\text{gas}} = \frac{k_{\text{gasmix}}}{A_{\text{gap}}(t)} \tag{17}$$

where k_{gasmix} is the conductivity of the gas mixture and $A_{\text{gap}}(t)$ is the time dependent gap width. Due to gap reduction, the internal pressure of the rod increases and may reach up to 100 atm at the end of life. This parameter may be of great influence when considering gaps next to be closed [10,11], as it will be shown later.

When the fuel and cladding surfaces are closer than a few mean free paths of the filling gas molecules, the gas temperature immediately adjacent to each surface is not the same as the surface temperature since a thermal jump appears on the wall that modifies the conductance of the medium. If a single gas of conductivity k_g is placed within two solid surfaces and a temperature gradient is established in the gas, the conductance of the gap is given by

$$h_{\text{gas}} = \frac{k_g}{A_{\text{gap}}(t) + J_c + J_f} \tag{18}$$

where J_c and J_f are the temperature jump distances. For each solid–gas interface they represent the distance from the interface where the extrapolation of the temperature gradient in the bulk of the gas intersects with the solid temperature (cladding and fuel, respectively in the case of a fuel rod). These distances depend on the material, the surface temperature, the gas pressure and accommodation parameters. For temperatures ranging from 150–300 °C, $J_c + J_f$ is 10^{-3} cm for He, 5×10^{-4} cm for Ar and less than 10^{-4} cm for Xe. The thermal accommodation coefficient of a single gas on a specific surface is defined as:

$$\alpha = \frac{T_r - T_0}{T_s - T_0} \leqslant 1 \tag{19}$$

where T_0 is the temperature of the molecules that strike the surface at temperature T_s and bounce with temperature T_r. If $T_r = T_s$, α is 1 and the reflected molecules are completely equilibrated with the surface.

Several authors propose a variety of models for the conductance between near surfaces when the gap between them is filled with a gas mixture as is the case for a fuel rod in operation [10,11,20,21]. The following expression was adopted in DIONISIO valid for a gap width similar to the mean roughness of both surfaces [10]:

$$h_{\text{gas}} = \sum_{i=1}^{n} \beta_i x_i \left(A_{\text{gap}}(t) + \frac{4}{\hat{\alpha}_i P} \left(\frac{\gamma_i - 1}{\gamma_i + 1} \right) \sqrt{\frac{\pi M_i T_{\text{gas}}}{2R}} \beta_i \right)^{-1} \tag{20}$$

where h_{gas} is in W cm^{-2} K^{-1}, T_{gas} and P are the temperature and internal pressure in the gap measured in K and Pa, respectively, the subscript i indicates the gases that compose the mixture, γ_i is the ratio of the specific heat coefficients at constant pressure and constant volume, M_i is the molecular weight of gas i and $\hat{\alpha}_i$ is the effective thermal accommodation coefficient of component i; it involves the individual accommodation coefficients between each solid surface and the gas phase in between. Each term of (20) has the shape given in (18); the second term within the parenthesis plays the role of $J_c + J_f$ for each component gas.

3.1.2. Radiation contribution

When the gap is open and the temperature is over 300 °C, it is necessary to consider the contribution of the radiation of each surface. An expression for this term is provided by Olander [11]

$$h_{\text{rad}} = \frac{4\lambda T^3}{(1/\varepsilon_c) + (1/\varepsilon_f) - 1} \tag{21}$$

where ε_j is the emissivity factor of each surface. The temperature used is the average between the external temperature of the fuel and the internal temperature of the cladding. $\lambda = 5.67 \times 10^{-8}$ W m^{-2} K^{-4} is the Stefan–Boltzmann's constant. The values of emissivity adopted are [21]:

$$\varepsilon_c = 0.1906 - 0.2166 \exp\left(-3.792 \times 10^{-3} T\right) \tag{22}$$
$$\varepsilon_f = 0.85$$

with T in the range (373–1900) K. For small gaps, the radiation influence is negligible as compared to that of conduction.

3.1.3. Solid–solid contact

When the rough pellet and cladding surfaces are in contact, heat transport occurs partly by solid conduction in the area of physical contact and by gas conduction in the remaining area. Fig. 2 represents the idealized phenomenon. The fraction of the surface area in contact depends on the way the deformation is produced (elastic or plastic), the compression stress, the internal pressure and the roughness of each surface. The mean thickness of the contact layer δ can be approximated by the sum of the mean roughness heights of both solids.

Different works analyze the contact conductance. The model proposed in [11] assumes the surface as constituted by cylindrical contact spots, each of radius R_1. If the unit area contains N cylinders, a unit cell of area $\pi R_2^2 = 1/N$ is associated to each spot. Analysis of heat transport in this idealized geometry, together with a number of assumptions (the fractional contact area $(R_1/R_2)^2$ increases with the interfacial pressure; the average radius of solid–solid contact, R_1, is proportional to the square root of the mean surface roughness, δ; and $R_1/R_2 \leqslant 1$) gives for the solid–solid contribution to gap conductance:

$$h_s = \frac{P_i}{H\delta} \left(\frac{2k_f k_c}{k_f + k_c} \right) \tag{23}$$

where P_i is the interfacial pressure and H is the Meyer hardness of the softer material.

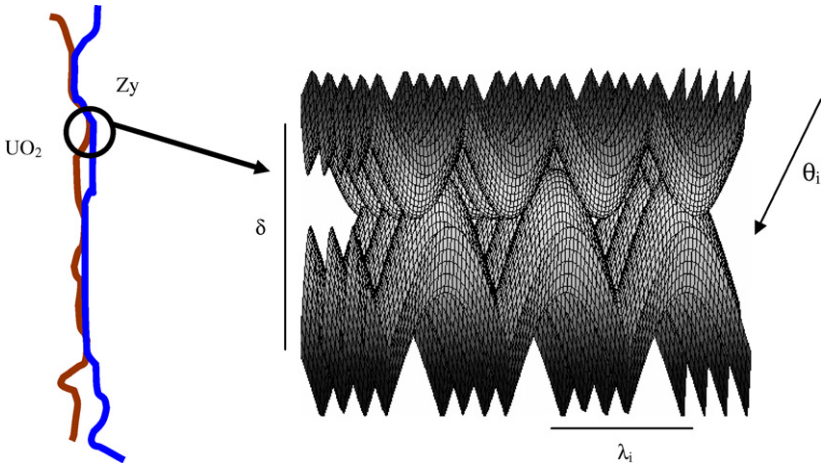

Fig. 2. Idealized scheme of two contact surfaces with different roughness. The crest height (δ) and slope (θ) as well as the distance between neighboring crests (λ) are indicated.

A more refined approximation is included in DIONISIO [22]. It is obtained taking the mean square value of roughness of both solids ($\sqrt{\delta_f^2+\delta_c^2}$, where δ_i represents the crest height of material i). With these hypotheses, the expression for the contact conductance is:

$$h_s = 1.45\left(\frac{2k_f k_c}{k_f+k_c}\right)\left(\frac{P_i}{H}\right)^n \frac{\sqrt{(\tan\theta_f)^2+(\tan\theta_c)^2}}{\sqrt{\delta_f^2+\delta_c^2}} \quad (24)$$

where $n = 0.5$ or 1 for elastic or plastic flow, $\tan\theta_i$ represents the average roughness slope of surface i and λ_i the spacing between neighboring crests, assumed regular for an ideal surface (see Fig. 2)

$$\tan\theta_i = \frac{2\delta_i}{\lambda_i}. \quad (25)$$

3.1.4. Validation of the model of thermal conductance

As stated before, the total gap conductance is given by the sum of three terms: $h_{fc} = h_{rad} + h_{gas} + h_s$ where $h_{rad} = 0$ if solid–solid contact is established and $h_s = 0$ if it is not. The presence of He in the gap introduces a singular behavior of the thermal conductance, especially for low pressures (lower than 2 atm) [21], as can be seen in Fig. 3. This condition is normally encountered at the beginning of fuel life, since He is used as rod filling gas. Unfortunately, no physical explanation has been given of this fact so far. The need of giving an accurate fitting of the measured results has induced us to finding an empirical expression for an extra term which is added to the gap conductance. The proposed expression is:

$$h_{add} = 4.69\times10^{-6}\exp(22.85x_{He}) \times \exp\left(-1.2\times10^{-4}(\delta_f+\delta_c)(P_{gas}-10)^2\right) \quad (26)$$

that depends on the internal gas pressure, P_{gas} in bar, and on the He fraction, x_{He}, in the mixture. It also considers the roughness of the cladding (δ_c) and pellet (δ_f) walls. Then

$$h_{fc} = h_{rad} + h_{gas} + h_s + h_{add}. \quad (27)$$

In Fig. 3 the experimental values of the gap conductance $h_{gap}(=h_{fc})$ reported in [21] vs. the internal gas pressure are shown together with the fitting obtained with Eq.

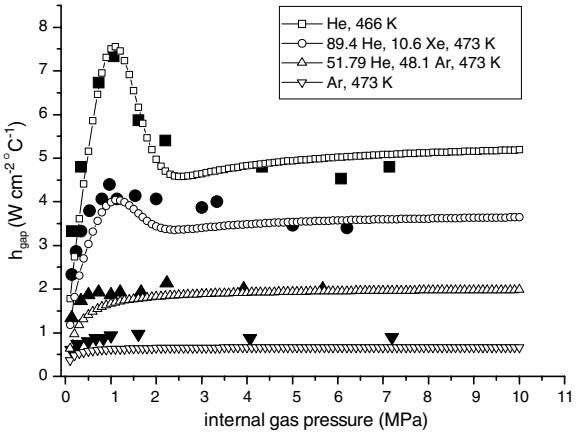

Fig. 3. Gap conductance vs. internal gas pressure for different mixtures.

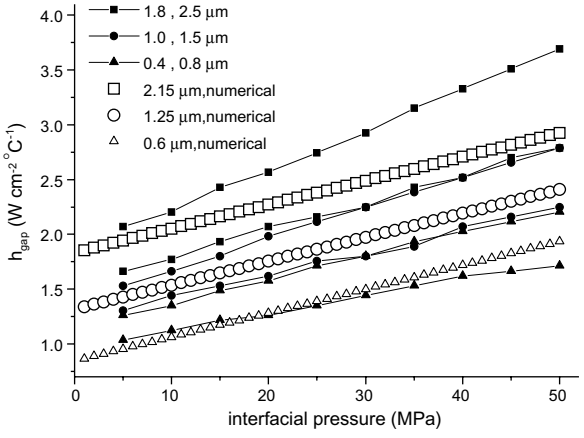

Fig. 4. Gap conductance vs. internal gas pressure for different roughness ranges.

(27). They correspond to gas mixtures with different proportions of He. A very good agreement is observed.

Fig. 4 shows the measured values of gap conductance vs. gas pressure for different mean roughness reported in [11]. The curves are grouped in pairs thus determining three roughness ranges: from 0.4 to 0.8 μm, from 1.0 to 1.5 μm and from 1.8 to 2.5 μm. The central value of each interval is chosen to run DIONISIO. The open points in Fig. 4 show the results of the simulations that, as expected, fall within the range of experimental values.

The good agreement between the experiments and the simulations led us to include the model of thermal conductance of the gap in the general code.

3.2. Mechanical contact

The numerical treatment of pellet-cladding mechanical interaction (PCMI) in DIONISIO is based on the analyses performed in Refs. [23–27]. It involves an algorithm based on Lagrange multipliers employing an irreducible formulation in each domain. The contact forces between two surfaces, generically denoted as source and receptor, are derived from the virtual works principle, assuming continuity for the displacements at the boundaries and imposing restrictions to avoid interpenetration of the surfaces. Starting from the applied external forces, the strain field is evaluated. Its magnitude allows deciding if the surfaces come into contact or not. Different contact conditions are considered: sticking contact (without friction), sliding contact (with friction), repeated contact and separation between bodies. Where the contact is produced, the basic condition of no overlap between the surfaces gives origin to contact forces that act on both bodies, of equal magnitude and opposite sense. The only possible effect of the normal components is compression. In contrast, the tangential components can produce sliding depending on the relative magnitudes of both components. According to the Coulomb's friction law, if there is no relative motion between the bodies when the contact is reached, no sliding takes place as long as the quotient tangential/normal components is lower than the static friction coefficient. If this limit is exceeded, sliding occurs. During motion, the magnitude of the tangential traction resisted by friction is governed by the dynamic friction coefficient.

In the finite element scheme employed, the contact condition is met when a boundary node of the source comes into contact with a receptor segment (limited by two nodes). Some of the nodes on the source surface can be in contact with receptor segments while others are still or again separated.

When the stress distribution of both surfaces is such that overlap between them had to occur, the contact subroutine performs a number of iterations until overlap is eliminated and the deformed surfaces are in contact. In the FEM formulation an incremental procedure is used [27]. The incremental potential of the contact forces is added to the incremental equilibrium equation. Starting from the stiffness and contact matrices and the nodal, external and contact force vectors at the iteration $i-1$, the incremental finite element equations of motion are formulated in matrix form:

$$\left(\begin{bmatrix} K^{i-1} & 0 \\ 0 & 0 \end{bmatrix} + \left[K_c^{i-1}\right]\right)\begin{bmatrix} \Delta U^i \\ \Delta\lambda^i \end{bmatrix} = \begin{bmatrix} R \\ 0 \end{bmatrix} - \begin{bmatrix} F^{i-1} \\ 0 \end{bmatrix} + \begin{bmatrix} R_c^{i-1} \\ \Delta_c^{i-1} \end{bmatrix} \tag{28}$$

ΔU^i	incremental displacement force vector in the ith iteration
$\Delta\lambda^i$	incremental contact force vector in the ith iteration
K^{i-1}	stiffness matrix in the $(i-1)$th iteration
K_c^{i-1}	contact stiffness matrix in the $(i-1)$th iteration
F^{i-1}	equivalent nodal point force vector in the $(i-1)$th iteration
R	total external force vector
R_c^{i-1}	contact force vector in the $(i-1)$th iteration
Δ_c^{i-1}	overlap displacement vector

Solution of the equations gives the increment in the displacement vector, the normal and tangential stress in each node and the corresponding increment in the contact forces for iteration i. This leads to the condition of sticking or sliding contact of surfaces, or separation. The number of equations depends on which condition is met.

Each node of the source boundary in contact condition contributes to the vectors K_c^{i-1}, R_c^{i-1} and Δ_c^{i-1} with two components, one for each global direction. For each source

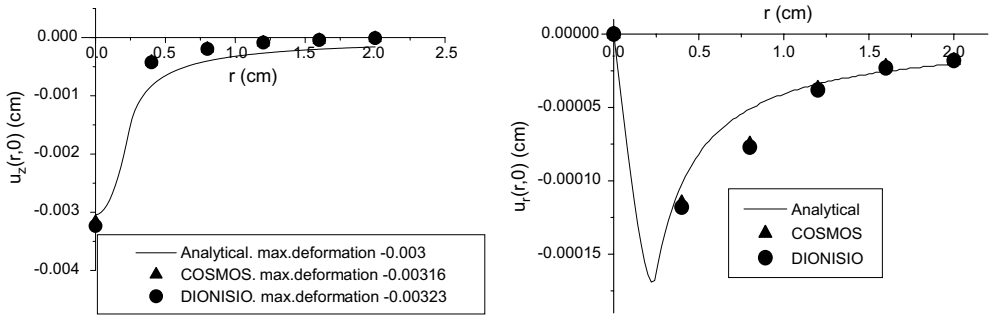

Fig. 5. Hertz problem of a sphere in contact with a plane. The origin of the coordinates r and z is placed at the initial contact point. Analytical and numerical results of the displacements u_r and u_z for $z = 0$.

node two receptor nodes (both ends of the element segment in contact) are involved. The parameter β indicates the location of the point of physical contact in units of the length of the receptor finite element segment. The final expression for these contributions is

$$\Delta_c^{i-1} = \begin{bmatrix} \Delta_x^{i-1} \\ \Delta_y^{i-1} \end{bmatrix}; \quad R_c^{i-1} = \begin{bmatrix} \lambda_x^{i-1} \\ \lambda_y^{i-1} \\ -(1-\beta)\lambda_x^{i-1} \\ -(1-\beta)\lambda_y^{i-1} \\ -\beta\lambda_x^{i-1} \\ -\beta\lambda_y^{i-1} \end{bmatrix}; \quad K_c^{i-1} = \Delta_c^{i-1} = \begin{bmatrix} \Delta_x^{i-1} \\ \Delta_y^{i-1} \end{bmatrix} \quad ; \quad R_c^{i-1} = \begin{bmatrix} \lambda_x^{i-1} \\ \lambda_y^{i-1} \\ -(1-\beta)\lambda_x^{i-1} \\ -(1-\beta)\lambda_y^{i-1} \\ -\beta\lambda_x^{i-1} \\ -\beta\lambda_y^{i-1} \end{bmatrix} \quad ; \quad K_c^{i-1} = \begin{bmatrix} 0 & & -1 & 0 \\ & & 0 & -1 \\ & & 1-\beta & 0 \\ & & 0 & 1-\beta \\ & & \beta & 0 \\ & 0 & 0 & \beta \\ \text{symmetric} & & 0 & 0 \\ & & 0 & 0 \end{bmatrix} \tag{29}$$

Upon assembly of the finite element equations, the general solution vector $\begin{bmatrix} \Delta U^i \\ \Delta \lambda^i \end{bmatrix}$ contains the displacements of all the nodes including those involved in the contact (i.e. that of the source and those of both ends of the receptor segment) as well as the increment of the components of the contact force. The algorithm has been derived for rectangular coordinates x, y but it is also applicable to problems with cylindrical symmetry in terms of the coordinates r and z, like that of the pellet-cladding interaction.

3.2.1. Validation of the model of mechanical contact

In order to check the correct performance of the model of mechanical contact, separate tests were carried out. To this end, this algorithm was employed to simulate the Hertz problem of a cylinder or a sphere in contact with a plane surface, for which the analytical solutions are known. The numerical approach involves plane strain for the cylinder and axial symmetry for the sphere. As an example, some results corresponding to the sphere are shown in Figs. 5 and 6 where the very good agreement between the values obtained with the algorithm described above, those calculated with the COSMOS package (version 1.85) and the analytical results can be recognized.

4. Code testing

The models of thermal and mechanical interaction described in Section 3. were incorporated to the previous version of the DIONISIO code that already contained the models for the many phenomena listed in Section 1. and tested in previous works [1,4,5].

4.1. FUMEX cases

DIONISIO 1.0 was used to simulate the experiments performed within the FUMEX 1 blind exercise. As an example of the results obtained, Fig. 7 shows the comparison between the experimental data and the predictions of the several codes that participated in the exercise [28] together with those of DIONISIO. The results obtained with DIONISIO are generally in good agreement with the experiments and in several cases are more accurate than those given by some other codes.

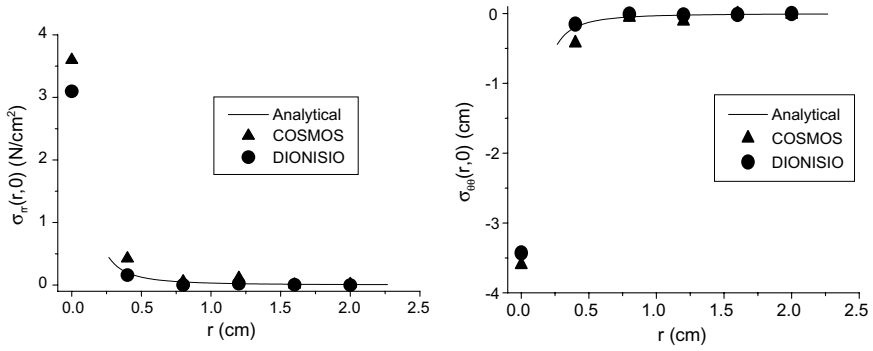

Fig. 6. Analytical and numerical results of the normal and tangential stress components in plane $z = 0$ for the same problem as in Fig. 5. The analytical curves are plotted outside the contact zone ($r > \approx 0.25$).

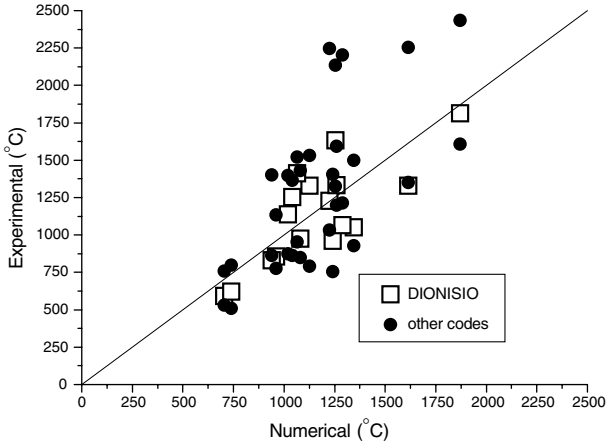

Fig. 7. Comparison between the FUMEX 1 experimental data and the numerical results obtained with DIONISIO and other codes for the center rod temperature.

4.2. Experiments with MOX fuels

DIONISIO was also compared with the experimental data obtained from the irradiation of the first argentine prototypes of MOX fuels for PHWR reactors [29]. The more remarkable feature evidenced in the post-irradiation examinations is the presence of ridges on the external surface of the cladding accompanying the pellets distribution.

The experimental data proceed from the rods identified as A.1.2 and A.1.3 which were subjected to different power histories. Fig. 8 shows the simulation with DIONISIO of the evolution with burnup of the radii of two rod sections (external cladding surface), one taken at the middle and the other at the top of the pellet (represented on the left hand side axis). The difference between them reveals the bamboo effect and is plotted (solid points) on the right hand side axis. Given the large uncertainties of the experimental results only a range of values of ridge height is reported in [29] for each rod: from 10 to 15 μm for rod A.1.2 and from 20 to 25 μm for rod A.1.3 (indicated as segments between two stars). A quite good agreement is observed between the values at the end and the reported values.

The evolution of the external pellet and internal cladding radii with burnup are represented in Fig. 9 by the solid and dotted lines, respectively, obeying the left hand side scale. On the right hand side the hoop stress is plotted. The instants when pellet-cladding contact is produced can be recognized by the coincidence of the solid and dotted lines. This is accompanied by a change of sign of the hoop stress revealing the appearance of a traction stress on the cladding. The predicted final gap width falls within the range of the experimental values, between 8 and 12 μm.

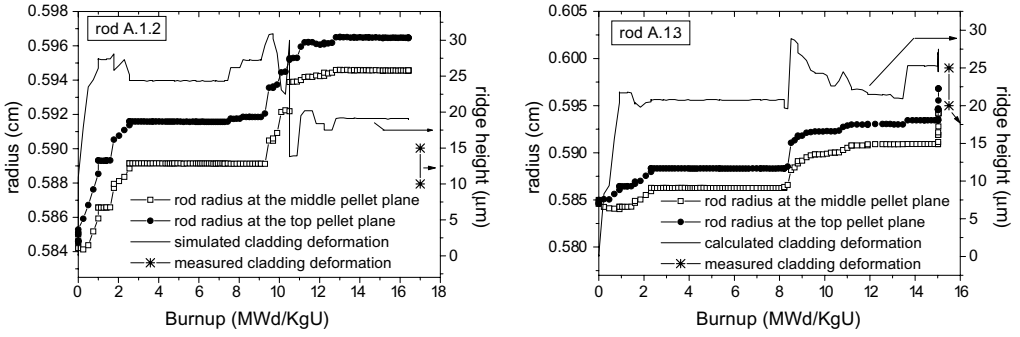

Fig. 8. Evolution with burnup of the rod(external cladding) radius at the top and middle plane for rods A.1.2 and A.1.3predicted by DIONISIO (left hand side scale). The stars indicate the range of values obtained in the experiment; the solid line gives the difference between the simulated radii (both sets plotted on the right hand side scale).

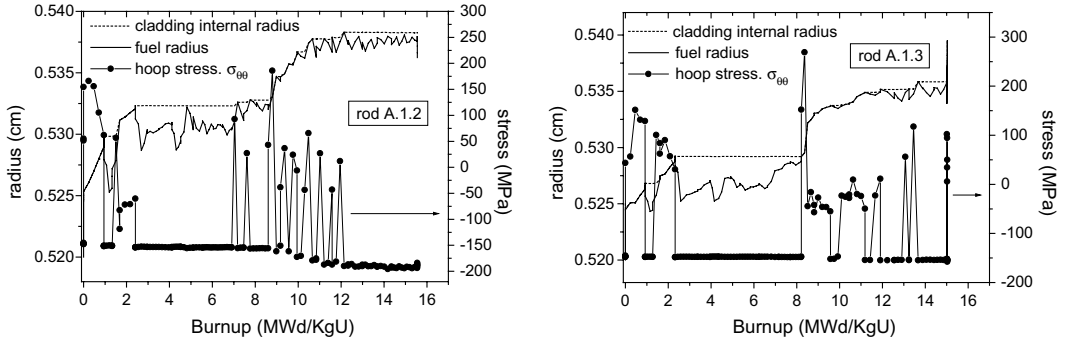

Fig. 9. Evolution with burnup of the pellet-cladding contact and the hoop stress for rods A.1.2 and A.1.3. The pellet and cladding radii are represented on the left axis and the stress on the right one.

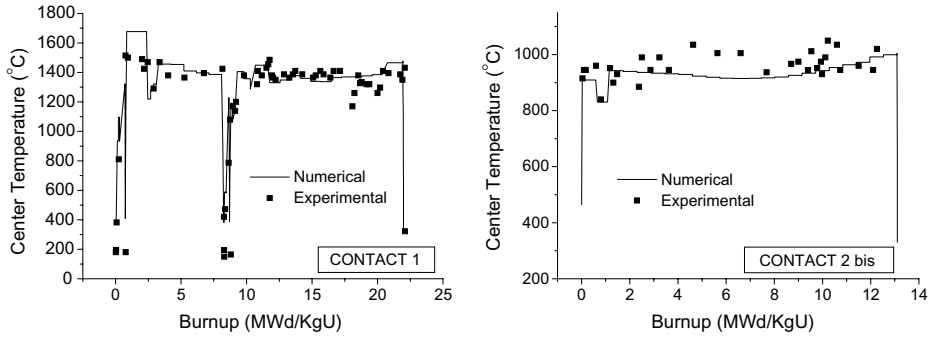

Fig. 10. Center temperature for CONTACT 1 and 2bis experiments.

4.3. The CONTACT experiment

The CONTACT series of experiments used short rods of Zry-4 clad-UO_2 pellets of typical PWR fuels that were irradiated in a pressurized water loop at a nearly constant power [30–32]. The CONTACT 1 rod was irradiated at a power level close to 40 kW/m and reached a discharge burnup of ~22 MWd/kgU; the internal pressure was 1 MPa of He. In CONTACT 2 the irradiation was performed at a power of 25 kW/m; the internal pressure was 0.1–0.2 MPa of He. At an early burnup of ~5.5 MWd/kgU a failure was detected, the rod was discharged and replaced with the rod CONTACT 2bis of identical design that reached a burnup of 12.4 MWd/kgU.

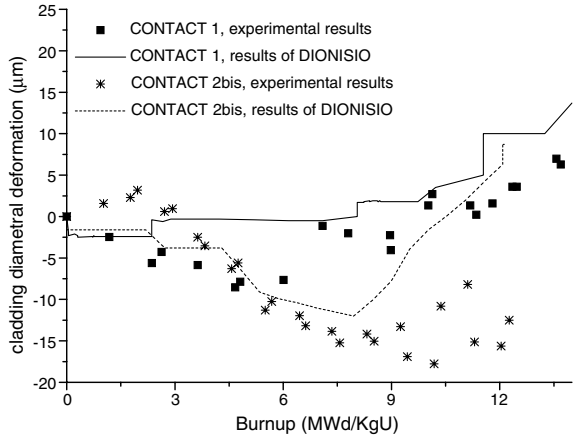

Fig. 11. Cladding deformation for CONTACT 1 and 2bis.

Fig. 10 shows the center temperature for CONTACT 1 and CONTACT 2bis and reveals the good prediction obtained with DIONISIO in both cases. The more demanding thermal conditions of experiment CONTACT 1 lead to a larger final clad deformation due to PCMI as compared with CONTACT 2bis, as can be seen in Fig. 11 where the experimental data and the predictions of DIONISIO are shown. Both experiments were instrumented with thermocouples for which reason a central hole was practiced in the fuel pellets. The quite large diametral contraction observed is probably due to material relocation until the fuel material collapses on the thermocouple wire [30]. This process is not simulated by DIONISIO because of lack of information. This is probably the cause of the departure between the simulation and the measured values. Nevertheless, the general trend is correctly reproduced by DIONISIO, particularly for the large values of burnup, when the effect of hole closure starts to be less important as compared with the rest of the phenomena involved, which are accounted for by the code.

Fig. 12 shows the internal cladding and pellet radii vs. burnup, together with the hoop stress. Like in the MOX experiments, positive values of the hoop stress are obtained

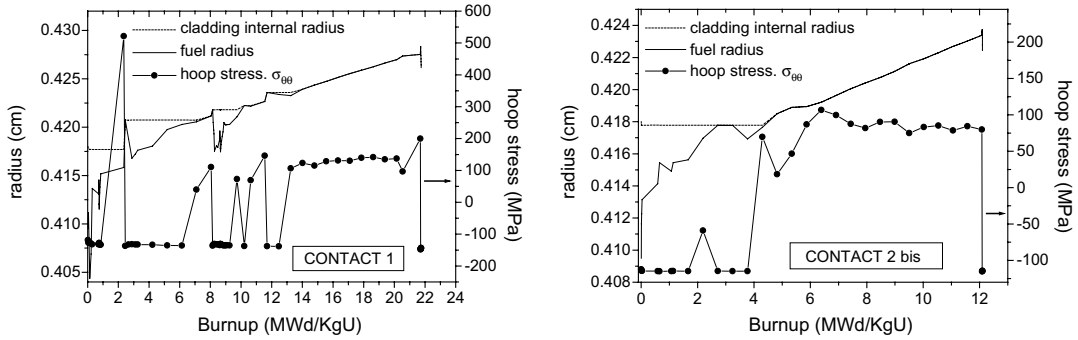

Fig. 12. Evolution with burnup of the pellet and cladding radii (left scale) and the hoop stress (right scale) for CONTACT 1 and 2bis.

Table 3
Numerical predictions vs. PIE measurements for the AECL bundles JR and NR

	JC		NC	
	Exp.	Num.	Exp.	Num.
FGR (cm^3)	48.3–60.6	42.52	39.1–42.6	34.15
FGR % Xe	0.8595	0.8471	0.8467	0.8413
Kr	0.0753	0.0941	0.1	0.0934
He	0.0413	0.0058	0.0479	0.0651
Ar	0.0193	0.0528	–	–
Ridge height (μm)	53–100	84	30–60	64
Final diameter (mm)	1.314–1.320	1.321–1.338	1.309–1.314	1.329–1.341
%Strain, mid plane	0.32–0.69	0.86	0.36–0.90	2.31
%Strain, ridge	1.16–2.1	2.15	(−)0.18–0.12	1.43
%Length increm.	0.083–0.24	0.97	0.055–0.095	0.27
Grain size (μm)				
External	8.5	10	–	10
Middle	29.75	32.5	–	24.5
Central	CG (0.47)	CG (0.56)	CG (0.435)	CG (0.56)

CG: columnar grain.

when pellet and cladding make contact. Its magnitude is smaller in the PWR than in the PHWR fuels due to the less demanding mechanical conditions.

4.4. AECL Bundles JC y NR

JC and NR were standard fuel bundles for the Bruce-A Ontario Hydro PHWR reactor [33]. The experiments were performed with pressurized light water as coolant under typical PHWR conditions of 9 to 10.5 MPa and 300°C. The enrichment of the UO_2 fuel was 1.55 and 1.44 wt% U^{235} for the JC and NR bundles, respectively; the cladding material was Zircaloy-4. The JR rods contained 90% Ar and 10% He as filling gas mixture at 1 atm of internal pressure. For the case of NR, three different rod designs were used: NR1 with no plenum, NR2 with a plenum of 8 mm (0.35 cm^3) and NR3 with a 12 mm plenum (0.58 cm^3). No element instrumentation was used during the irradiation but all the rods were subjected to extensive post-irradiation examination (PIE) that comprised dimensional changes, fission gas release, fuel burnup analysis, and metallography that included grain size measurement. These experiments were simulated with DIONISIO. The numerical predictions and the PIE results are compared in Table 3. The agreement is good in general although a slight tendency of DIONISIO to overestimating deformations is recognized.

5. Discussion and conclusions

Simulation of PCMI is a complex task not only because of the numerical difficulties involved but also because it is connected with the wide variety of physical and chemical phenomena that take place within the rod. In particular, the quality of the thermal predictions is determinant of the accuracy of the whole simulation. The model of thermal conductance of the gap included in DIONISIO considers the contributions of radiation, conduction through the gas mixture, solid contact between rough surfaces and a correction for low gas pressures. The models and parameters involved in these descriptions were taken from the literature, except for the latter which was developed by this working group.

The model of mechanical contact included in DIONISIO allowed a more than acceptable description of the bamboo effect and the radial cladding deformation in all the cases simulated.

Each algorithm was separately tested and successfully compared with data available in the literature. With these models included in DIONISIO, the code was applied to the simulation of irradiation experiments of rods of diverse characteristics. The agreement with the measured values is satisfactory, revealing the accuracy of the individual models and the adequate coupling among them.

The running time of DIONISIO depends on the number of steps in which the power history is divided. In a standard case it is about 20 min with a PENTIUM III processor of 700 MHz. The program is written in the FORTRAN language.

References

[1] A. Denis, A. Soba, Nucl. Eng. Des. 223 (2003) 211.
[2] L. Caillot, B. Linet, C. Lemaignan, in: Proc. SMIRT 12, Stuttgart, Germany, 1993.
[3] J. MathewsAdvances in Nuclear Science and Technology, vol. 6, Academic Press, 1972.
[4] A. Denis, R. Piotrkowski, J. Nucl. Mater. 229 (1996) 149.
[5] A. Denis, R. Piotrkowski, IAEA-TECDOC-957 (1997) 455.
[6] S. Glasstone, A. Sesonske, Ingeniería de reactors nucleares, Ed. Reverté, 1968, pp.375.
[7] D.R. Olander, Pure & Appl. Chem. 67 (6) (1995) 1003–1010.
[8] F. Nagase, T. Otomo, H. Uetsuka, J. Nucl. Sci. Technol. 40 (4) (2003) 213.
[9] L.J. Segerlind, Applied Finite Element Analysis, 2nd ed., Wiley, 1984.
[10] Handbook of materials properties for use in the analysis of light water reactor fuel behavior, MATPRO version 11, NUREG/CR-0497, TREE–1280, 1979.

[11] D.R. Olander, Technical Information Center (1976).
[12] Kinoshita, Ichikawa, Nucl. Eng. Des. 56 (1980) 49.
[13] J.K. Fink, L. Leibowitz, J. Nucl. Mater. 226 (1995) 44.
[14] G. Delete, M.Charles, Water Reactor Fuel Element Modelling at High Burnup and its Experimental Support, IAEA–TECDOC–957, IAEA (1997) p. 203.
[15] A. Levy, B. Pifko, Int. J. Num. Meth. Eng. 17 (1981) 747.
[16] G.A. Berna et al., NUREG/CR-1845 (1980).
[17] A. Marino, E. Savino, S. Harriague, J. Nucl. Mater. 229 (1996) 155.
[18] A. Soba, MECON, 2005.
[19] S. Wahid, Madhusudana, Int. J. Heat Transf. 43 (2000) 4483.
[20] L. Tong, J. Weisman, Thermal analysis of pressurized water reactors, American Nuclear Society, La Grange Park, Illinois, USA, 1995.
[21] J. Ainscough, OECD, NEA, April 1982.
[22] G. Jacobs, N. Todreas, Nucl. Sci. Eng. 50 (1973) 283.
[23] F.J. Gallego, J.J. Anza, Métodos Numéricos para Cálculo y Diseño en Ingeniería 5 (2) (1989) 163.
[24] U. Sellgren, S. Björklund, S. Andersson, Wear 254 (2003) 1180.
[25] J. Zurita, M. Doblarey, L. García, Métodos Numéricos para Cálculo y Diseño en Ingeniería 9 (1) (1993) 15.
[26] K. Bathe, A. Chaudhary, Int. J. Num. Meth. Eng. 21 (1985) 65–88.
[27] K. Bathe, Finite Element Procedures, Prentice Hall, 1996.
[28] Fuel Modeling at extended burnup, IAEA–TECDOC–998, IAEA, 1998.
[29] A. Marino, E. Pérez, P. Adelfang, J. Nucl. Mater. 229 (1996) 169.
[30] J.A. Turnbull, IFPE/CONTACT Rev.1. Database for CONTACT experiments irradiated at CEA Grenoble, October 1998.
[31] M. Bruet, J. Dodalier, P. Melin, M.Pointud, IAEA Specialists' Meeting on Water Reactor Fuel Elements Performance Computer Modelling, Blackpool, UK, March 1980.
[32] M. Charles, C. Lemaignan, J. Nucl. Mater. 188 (1992) 96.
[33] V.I. Arismesku, NEA-1596 IFPE/AECL-BUNDLE, Chalk River, Ontario, Canada, 2000.